European Spine Journal (2019) 28:1783–1792
https://doi.org/10.1007/s00586-019-05984-5

ORIGINAL ARTICLE

Noise-optimised virtual monoenergetic imaging of dual-energy CT: effect on metal artefact reduction in patients with lumbar internal fixation

Yanwei Zeng[1,2] · Kai Deng[3] · Haitao Yang[3] · Yi Tan[3] · Jun Liu[3] · Daoying Geng[1,2] · Jun Zhang[1,2]

Received: 19 November 2018 / Revised: 9 April 2019 / Accepted: 19 April 2019 / Published online: 30 April 2019

Abstract

Purpose The purpose of this study was to evaluate the effects of noise-optimised virtual monoenergetic imaging (VMI+) reconstructions on reducing metal artefacts compared to traditional virtual monoenergetic imaging (VMI) and linearly blended (M_0.6) reconstructions in patients with lumbar metal internal fixation in dual-energy CT (DECT).

Methods Forty patients who underwent DECT were evaluated in this retrospective study. Images were reconstructed with M_0.6 and with VMI+ and VMI at 10-keV intervals from 40 keV to 190 keV. Attenuation and noise were measured in the hyperdense artefacts, hypodense artefacts, spinal canal, abdominal aorta (AA), and inferior vena cava (IVC). An artefact index (AI) was calculated. A subjective evaluation of the metal–bone interface, surrounding soft tissue, spinal canal, AA, and IVC was conducted.

Results The AI values for the hypodense artefacts, spinal canal, and IVC were lowest in the 130 keV VMI+ series, for the hyperdense artefacts in the 120 keV VMI+ series, and for the AA in the 190 keV VMI+ series. Except for the hypodense artefacts, the AI values were lower compared to the M_0.6 images and all the VMI series (all $p < 0.05$). The subjective image quality was highest at 130 keV VMI+ for the metal–bone interface, surrounding soft tissue, AA, and IVC, and at 120 keV VMI+ for the spinal canal. Except for the AA, these rating scores were higher compared to the M_0.6 images and the entire VMI series (all $p < 0.05$).

Conclusions DECT with high-keV VMI+ efficiently reduces metal artefacts and shows superior image quality in patients with lumbar internal fixation.

Graphical abstract

These slides can be retrieved from Electronic Supplementary Material.

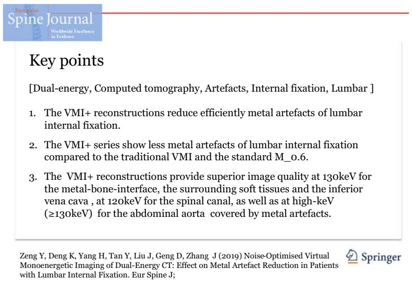

European Spine Journal
Worldwide Excellence in Evidence

Key points

[Dual-energy, Computed tomography, Artefacts, Internal fixation, Lumbar]

1. The VMI+ reconstructions reduce efficiently metal artefacts of lumbar internal fixation.
2. The VMI+ series show less metal artefacts of lumbar internal fixation compared to the traditional VMI and the standard M_0.6.
3. The VMI+ reconstructions provide superior image quality at 130keV for the metal-bone-interface, the surrounding soft tissues and the inferior vena cava , at 120keV for the spinal canal, as well as at high-keV (≥130keV) for the abdominal aorta covered by metal artefacts.

Zeng Y, Deng K, Yang H, Tan Y, Liu J, Geng D, Zhang J (2019) Noise-Optimised Virtual Monoenergetic Imaging of Dual-Energy CT: Effect on Metal Artefact Reduction in Patients with Lumbar Internal Fixation. Eur Spine J;

Springer

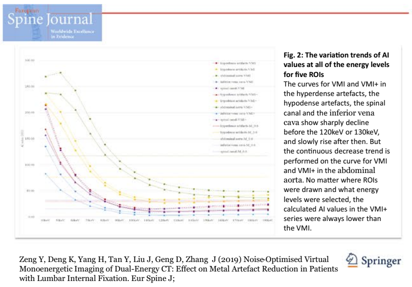

European Spine Journal
Worldwide Excellence in Evidence

Fig. 2: The variation trends of AI values at all of the energy levels for five ROIs
The curves for VMI and VMI+ in the hyperdense artefacts, the hypodense artefacts, the spinal canal and the inferior vena cava show sharply decline before the 120keV or 130keV, and slowly rise after then. But the continuous decrease trend is performed on the curve for VMI and VMI+ in the abdominal aorta. No matter where ROIs were drawn and what energy levels were selected, the calculated AI values in the VMI+ series were always lower than the VMI.

Zeng Y, Deng K, Yang H, Tan Y, Liu J, Geng D, Zhang J (2019) Noise-Optimised Virtual Monoenergetic Imaging of Dual-Energy CT: Effect on Metal Artefact Reduction in Patients with Lumbar Internal Fixation. Eur Spine J;

Springer

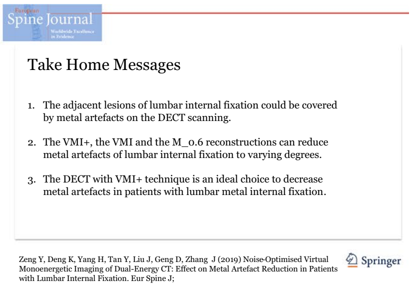

European Spine Journal
Worldwide Excellence in Evidence

Take Home Messages

1. The adjacent lesions of lumbar internal fixation could be covered by metal artefacts on the DECT scanning.
2. The VMI+, the VMI and the M_0.6 reconstructions can reduce metal artefacts of lumbar internal fixation to varying degrees.
3. The DECT with VMI+ technique is an ideal choice to decrease metal artefacts in patients with lumbar metal internal fixation.

Zeng Y, Deng K, Yang H, Tan Y, Liu J, Geng D, Zhang J (2019) Noise-Optimised Virtual Monoenergetic Imaging of Dual-Energy CT: Effect on Metal Artefact Reduction in Patients with Lumbar Internal Fixation. Eur Spine J;

Springer

Yanwei Zeng and Kai Deng contributed equally to this work.

Electronic supplementary material The online version of this article (https://doi.org/10.1007/s00586-019-05984-5) contains supplementary material, which is available to authorized users.

Extended author information available on the last page of the article

Keywords Dual-energy · Computed tomography · Artefacts · Internal fixation · Lumbar

Introduction

Metal internal fixations for lumbar diseases such as vertebral fractures, disc herniation, spinal stenosis, and spondylolisthesis are widely used in surgery. In patients with these implants, computed tomography (CT) scanning is always an appropriate choice for post-operative evaluation [1, 2]. However, it is disruptive to assess the fixation itself, the interface between the fixation and the vertebra, and the peripheral structure because of the artefacts caused from the metal implant [3]. Furthermore, some surgical complications might be missed by CT diagnosis due to the interference of metal artefacts, including the breakage, loosening, or removal of internal fixation, and infection, damage, or haematoma of the nearby muscles, nerves, and blood vessels [4–8], especially after abdominal aortic injury, which could lead to life-threatening bleeding.

Metal artefacts occur due to two main physical phenomena, namely beam-hardening and photon starvation, which principally generate hyper- and hypodense streaks [3, 9, 10]. To minimise the metal artefacts on images, several methods have been used in multidetector CT scanning and image post-processing. These methods involve increasing the peak voltage and tube charge, using narrow detector collimation, acquiring thin sections, and selecting an appropriate reconstruction algorithm [11]. In recent years, dual-energy CT (DECT) derived virtual monochromatic imaging (VMI) has played an important role in minimising metal artefacts [2, 3, 8, 9, 12–17]. More recently, a noise-optimised virtual monoenergetic imaging (VMI+) technique at low keV levels has been introduced to maximise image quality for tumorous and vascular imaging compared to traditional VMI and linearly blended (M_0.6) reconstructions [18–25]. However, the application of the VMI+ technique to decrease metal artefacts has not yet been evaluated.

Thus, the aim of this study was to assess the effect of DECT with the VMI+ reconstruction technique on reducing metal artefacts by evaluating quantitative and qualitative image quality compared to traditional VMI and linearly blended (M_0.6) reconstructions in patients with metal lumbar internal fixation.

Materials and methods

Patient population

This retrospective study was approved by the institutional review board of the Second Xiangya Hospital of Central South University through written informed consent.

Exclusion criteria were internal fixations placed on only one side of the spine ($n=1$), obvious motion artefacts in the original images ($n=1$), patients under 18 years of age ($n=3$), and enhanced CT scans ($n=0$). And then this study analysed 40 consecutive patients (50.5 ± 14.1 years; range 18–76 years) (Table 1), including 23 men (45.7 ± 14.0 years; range, 18–70 years) and 17 women (57.1 ± 11.8 years; range 35–76 years) who underwent a DECT examination after lumbar implant surgery between January 2017 and October 2017. A total of 30 AA with hypodense streaks and 31 IVC with hyperdense streaks were chosen from the 40 cases for subsequent evaluation.

DECT image acquisition

All the CT examinations of the lumbar spine were performed using a third-generation dual-source DECT scanner (SOMATOM Force, Siemens Healthcare, Erlangen, Germany). Tube voltages in the dual-energy mode were set

Table 1 Patient characteristics

Parameters	Values
Number of patients	40
Male-to-female ratio	23:17
Age (range) years	50.5 ± 14.1 (18–76)
Titanium alloys material (definite/indefinite)	31/9
Reasons of operation	
Slipped disc	22
Spinal stenosis	17
Spondylolisthesis	10
Intraspinal tumour	1
Scoliosis	2
Vertebral fractures	5
Spinal tuberculosis	4
Reasons of CT scanning	
Post-operative evaluation	31
Post-operative lumbago	3
Peripheral motor neurologic symptoms	2
Post-operative infection symptoms	2
Evaluation before taking-fixation	2

as follows: tube A 90 kV, 190 mAs per rotation; and tube B Sn 150 kV with tin filter, 380 mAs per rotation. Other parameters were slice acquisition of 1 × 128 × 0.6 mm, pitch of 0.5, and rotation time of 0.5 s.

DECT data reconstruction

Reconstructions of the dual-energy data were performed on a 3D multi-modality workstation (syngo.via, version VA30A, Siemens) with a bone convolution kernel (Qr40, Siemens) and an iterative reconstruction technique (ADMIRE, Siemens; strength level, 2). The novel VMI+ and traditional VMI were reconstructed at 40–190 keV levels at 10-keV intervals. Overall, 60% of the low- and 40% of the high-kV data were merged to approximate the appearance of a traditional single-energy CT at M_0.6. All the images were reconstructed as axial slices with 1.0 mm thickness and interval and displayed using a standard bone window (width 1500 HU, level 450 HU).

Quantitative image analysis

For the objective analysis, one radiologist (D. K with 4 years of experience in CT) who did not participate in subjective image analysis reviewed all the image series on a multi-modality workstation (syngo.via, Siemens). Measuring the signal attenuation in mean HU and image noise defined as the standard deviation (SD) were performed by placing regions of interest (ROIs) in the M_0.6 images as well as the VMI and VMI+ series (both at 40–190 keV at 10-keV intervals). At the worst level obstructed by the metal artefacts of each patient, five ROIs were drawn around the metal implant, and one background ROI less disturbed by the artefacts was put in the fat. The six ROIs were selected as follows (Fig. 1): (1) hyperdense artefacts (left psoas major muscles, 100 mm^2), (2) hypodense artefacts (left erector spinae muscles, 40 mm^2), (3) spinal canal (40 mm^2), (4) AA (40 mm^2), (5) IVC (20 mm^2), and (6) subcutaneous fat of the back (40 mm^2). The six ROIs were, respectively, placed at the same location and were of the same size in all the image series of each patient. To decrease the measurement error, the radiologist performed the measurements twice and averaged the results.

To quantify the severity of the artefacts, an artefact index (AI) was calculated according to a prior study using the formula [13] $\mathrm{AI} = \sqrt{SDa^2 - SDb^2}$. SDa represents the noise of an ROI around a metal implant, and SDb is the noise of a fat ROI measured at the same level. If SDa < SDb, 0 was recorded as the AI value.

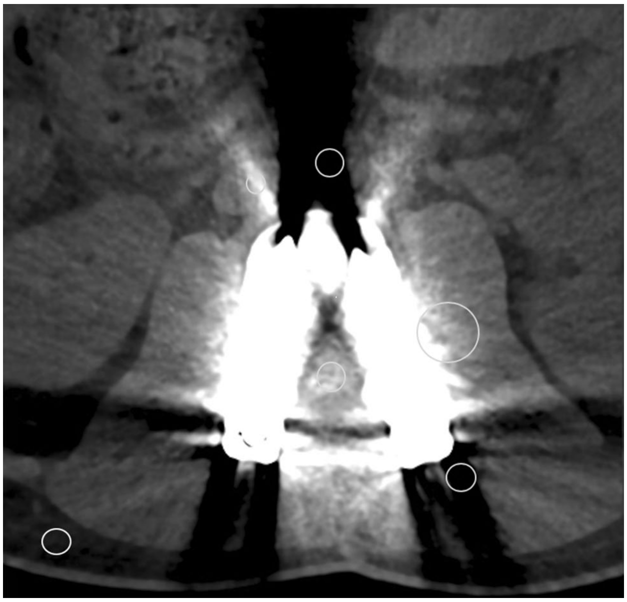

Fig. 1 The places of six ROIs. Six ROIs were placed in the hyperdense artefacts (left psoas major muscles), the hypodense artefacts (left erector spinae muscles), the spinal canal, the AA, the IVC and the subcutaneous fat of the back, respectively

Qualitative image analysis

For the subjective analysis, three radiologists (Y. HT, Z. J and L. J with 2, 10, and 13 years of experience in spinal radiology, respectively) blinded to the image reconstruction techniques independently assessed the M_0.6 images as well as the VMI and VMI+ series (40–190 keV, at 10-keV intervals) of each patient in random order. The radiologists were allowed to freely adjust the window setting. To prevent recall bias, there was at least a 1-week interval between the evaluations of each image series. Totally, 33 weeks were spent on the subjective evaluation.

The three radiologists rated each image series using a 5-point Likert scale as follows [9]: metal–bone interface (ranging from 1 = unobservable to 5 = clear); surrounding soft tissue (mainly including the paravertebral muscles and the abdominal viscera), spinal canal, AA, and IVC (ranging from 1 = extensive artefacts with non-diagnostic assessment to 5 = hardly perceptible artefacts with fully diagnostic assessment).

Statistical analysis

Statistical software (IBM SPSS Statistics, version 25.0, IBM, Armonk, NY, USA) was used to perform the statistical analyses. Variables are reported as mean ± standard deviation. A p value less than 0.05 was considered statistically significant.

The normal distribution of the data was assessed using the Kolmogorov–Smirnov test. The analysis of variance (ANOVA) test was performed for normally distributed data. The Wilcoxon matched pairs test was implemented for the failing normality test [26].

The intraclass correlation coefficient (ICC) for evaluating the agreement among the three observers was interpreted as follows: ICC < 0.20, scarce agreement; ICC 0.21–0.40, less agreement; ICC 0.41–0.60, moderate agreement; ICC 0.60–0.80, strong agreement; ICC 0.81–1.0, almost identical agreement.

Results

Radiation dose

The average cumulative CT dose index (CTDIvol) and dose length product (DLP) of all the examinations were 15.66 ± 0.83 mGy (range 14.06–17.61 mGy) and 499.98 ± 61.90 mGy * cm (range 379.00–612.40 mGy * cm).

Quantitative image analysis

Artefact index The minimum AI values for the hyperdense artefacts were found at 120 keV in the VMI+ series (11.07 ± 6.34). Although no significant differences were found compared to 110–140 keV VMI+ ($p \geq 0.607$), these AI values were significantly lower compared to the M_0.6 series (29.68 ± 15.87, $p < 0.001$) and all the VMI datasets ($p \leq 0.015$).

In the hypodense artefacts, the calculated AI values were lowest in the 130 keV VMI+ (27.64 ± 13.60) and 120 keV VMI (33.40 ± 12.80) series without significant differences ($p = 0.055$), but were both significantly lower compared to the M_0.6 series (76.49 ± 42.29, both $p < 0.001$).

The calculated spinal canal AI values were lowest in the 130 keV VMI+ series (9.95 ± 6.41), and the differences compared to 110–150 keV VMI+ were not significant ($p \geq 0.381$), but all the AI values in these algorithms were lower compared to the M_0.6 series (32.50 ± 23.09, $p < 0.001$) and all the VMI datasets ($p \leq 0.024$).

Similarly, the calculated AI values for the IVC were also lowest for VMI+ at 130 keV (3.75 ± 4.89), and there were no significant differences compared to 110–150 keV VMI+ ($p \geq 0.053$). In comparison with the M_0.6 series (15.71 ± 12.49, $p < 0.001$) and all the VMI datasets ($p \leq 0.009$), the 110–150 keV VMI+ series showed significantly lower AI values.

The VMI+ reconstructions had the lowest AI values at 190 keV (36.90 ± 39.92) for the AA. Compared to the M_0.6 series (117.60 ± 84.34, $p < 0.001$) and all the other monoenergetic image datasets ($p \leq 0.001$), the AI values for VMI+ at 190 keV were significantly lower.

The results of the calculated AI values are summarised in Table 2 and Fig. 2.

Attenuation and noise The highest attenuations for the hyperdense artefacts, spinal canal, and IVC were observed at the 40 keV energy level in all the VMI and VMI+ series, which were higher than the attenuations measured at M_0.6, and a negative trend then appeared with increasing energy levels. Conversely, the lowest attenuations were measured at the 40 keV energy level for VMI and VMI+ in the hypodense artefacts and the AA with an incremental trend and lower than the M_0.6 images.

In the hyperdense artefacts, hypodense artefacts, spinal canal, and IVC, the image noise markedly decreased from 40 keV to 120 keV or 130 keV in the VMI+ series, and gradually increased after the lowest level. However, the image noise of the AA subsequently decreased with increasing energy levels. The variation trends in image noise in the five ROIs were all similar to the AI values. Compared to the M_0.6 and VMI series at corresponding energy levels, the image noises were significantly lesser for VMI+ at the same energy level with the least noise in all the ROIs ($p < 0.001$ and $p \leq 0.014$, respectively).

Qualitative image analysis

Subjective evaluations of the metal–bone interface (mean 4.60; ICC 0.704) and the surrounding soft tissues (mean 4.45; ICC 0.608) were both best in the 130 keV VMI+ series with high agreement and were all significantly superior than the other monoenergetic image datasets ($p \leq 0.009$ and $p \leq 0.001$, respectively) and M_0.6 reconstructions (all $p < 0.001$).

The ratings of the spinal canal peaked at 120 keV VMI+ with high agreement (mean 4.87; ICC 0.639), and significantly better ratings were observed compared to the other monoenergetic image datasets ($p \leq 0.021$) and M_0.6 reconstructions ($p < 0.001$).

The most optimal scores for the IVC were found in the 130 keV VMI+ series with high agreement (mean 4.50; ICC 0.762), and there were no significant differences compared to 120 keV VMI+ (mean 4.35; ICC, 0.863; $p = 0.100$). However, there were also no significant differences between 120 keV VMI+ and 130 keV VMI (mean, 4.27; ICC, 0.749; $p = 0.253$). Furthermore, 130 keV VMI+ had superior ratings compared to all the other monoenergetic images with the exception of the 120 keV VMI+ and M_0.6 datasets ($p \leq 0.001$ and $p < 0.001$, respectively).

For the subjective evaluation of the AA, the highest scores were in the 130 keV VMI+ series with almost identical agreement (mean, 4.03; ICC, 0.864) and significantly higher than the M_0.6 series ($p \leq 0.001$), but showed no significant

Table 2 Results of AI values on the quantitative evaluation

AI (HU)	ROIs				
	Hyperdense artefacts	Hypodense artefacts	AA	IVC	Spinal canal
M_0.6	29.68 ± 15.87	76.49 ± 42.29	117.60 ± 84.34	15.71 ± 12.49	32.50 ± 23.09
VMI 40	214.44 ± 111.06	237.31 ± 155.02	269.41 ± 207.90	135.48 ± 84.53	206.86 ± 103.91
VMI+ 40	168.40 ± 88.32	217.16 ± 102.18	237.89 ± 180.11	83.77 ± 60.67	157.25 ± 75.38
VMI 50	132.11 ± 69.63	201.62 ± 109.54	276.70 ± 150.46	82.10 ± 54.08	128.60 ± 77.93
VMI+ 50	105.74 ± 55.11	179.87 ± 67.63	235.61 ± 132.67	52.72 ± 38.34	102.43 ± 55.39
VMI 60	81.78 ± 45.42	146.13 ± 83.71	242.59 ± 133.83	49.51 ± 35.85	80.03 ± 50.91
VMI+ 60	67.35 ± 34.99	129.11 ± 57.52	205.88 ± 118.81	33.55 ± 24.93	66.70 ± 36.91
VMI 70	52.45 ± 29.09	97.93 ± 58.19	188.06 ± 115.03	29.63 ± 25.05	49.14 ± 32.57
VMI+ 70	43.99 ± 22.52	88.41 ± 43.10	160.32 ± 103.12	21.36 ± 16.94	44.16 ± 24.47
VMI 80	34.23 ± 19.21	66.39 ± 38.13	139.34 ± 89.34	18.08 ± 17.59	30.45 ± 20.83
VMI+ 80	29.86 ± 14.51	61.52 ± 29.59	120.22 ± 82.38	13.88 ± 11.85	29.84 ± 17.05
VMI 90	23.87 ± 12.22	48.06 ± 25.05	107.52 ± 73.77	11.89 ± 12.19	20.44 ± 12.38
VMI+ 90	20.16 ± 9.31	44.21 ± 20.08	93.65 ± 69.78	8.35 ± 8.39	19.80 ± 11.91
VMI 100	18.48 ± 8.05	38.57 ± 16.79	86.38 ± 64.14	9.08 ± 9.17	15.67 ± 7.72
VMI+ 100	14.80 ± 6.72	34.60 ± 14.58	75.41 ± 61.56	5.35 ± 6.31[b]	14.27 ± 8.09
VMI 110	16.12 ± 7.27	34.37 ± 13.28	72.51 ± 57.68	8.64 ± 7.52	14.71 ± 6.31
VMI+ 110	11.72 ± 6.60[ab]	29.54 ± 13.16[a]	62.47 ± 56.36	4.02 ± 5.35[ab]	11.20 ± 6.57[ab]
VMI 120	16.01 ± 7.88	33.40 ± 12.80[a]	63.34 ± 53.32	9.26 ± 6.92	15.87 ± 6.43
VMI+ 120	**11.07 ± 6.34**[b]	27.70 ± 13.31[a]	53.35 ± 52.87	3.77 ± 4.88[ab]	10.14 ± 5.89[ab]
VMI 130	17.10 ± 8.06	34.21 ± 12.98	57.38 ± 50.10	10.52 ± 6.48	17.56 ± 7.02
VMI+ 130	11.22 ± 6.76[ab]	**27.64 ± 13.60**	47.58 ± 49.61	**3.75 ± 4.89**[b]	**9.95 ± 6.41**[b]
VMI 140	18.18 ± 8.59	35.85 ± 13.04	53.86 ± 47.45	11.44 ± 6.72	19.30 ± 7.84
VMI+ 140	11.84 ± 7.09[ab]	28.85 ± 13.44[a]	43.75 ± 47.00	4.25 ± 5.03[ab]	10.52 ± 6.65[ab]
VMI 150	19.22 ± 9.03	37.59 ± 13.22	51.66 ± 45.37	12.31 ± 6.90	20.78 ± 8.59
VMI+ 150	12.71 ± 7.13[a]	29.68 ± 13.68[a]	41.49 ± 44.64[b]	4.58 ± 5.36[ab]	11.28 ± 7.00[ab]
VMI 160	20.11 ± 9.49	38.85 ± 13.88	50.39 ± 43.72	13.10 ± 7.12	22.00 ± 9.29
VMI+ 160	13.54 ± 7.18[a]	30.76 ± 13.81[a]	39.82 ± 42.92[b]	4.93 ± 5.65[b]	11.94 ± 7.43[a]
VMI 170	21.28 ± 9.16	40.51 ± 13.93	49.57 ± 42.45	13.70 ± 7.36	23.21 ± 9.50
VMI+ 170	14.33 ± 7.09	31.74 ± 14.02[a]	38.55 ± 41.65[b]	5.16 ± 5.94[b]	12.51 ± 7.85[a]
VMI 180	22.06 ± 9.31	41.66 ± 14.33	49.42 ± 41.34	14.18 ± 7.59	23.92 ± 9.99
VMI+ 180	14.96 ± 7.20	32.58 ± 14.26[a]	37.62 ± 40.70[b]	5.55 ± 6.10[b]	13.04 ± 8.13
VMI 190	23.30 ± 9.84	42.66 ± 14.69	48.67 ± 40.82	14.69 ± 7.64	24.88 ± 10.25
VMI+ 190	15.48 ± 7.33	33.30 ± 14.44[a]	**36.90 ± 39.92**[b]	5.82 ± 6.28[b]	13.51 ± 8.48

Data are reported as mean ± standard deviation in all of the monoenergetic series and the M_0.6 reconstructions for five ROIs

Bold fonts hint the lowest AI value in all of the image series for each ROI

[a] No significant difference compared to the lowest AI value

[b] Significant difference of lower AI value compared to the M_0.6 images and all of the VMI series

differences compared to the 140–170 keV VMI+ and 150 keV VMI series (all $p \geq 0.082$).

The results of the qualitative image assessment are shown in Table 3. Images of a patient at M_0.6, 40 keV and 130 keV VMI, and VMI+ are shown in Fig. 3.

Discussion

This study evaluated the effects of reducing metal artefacts and improving image quality using DECT VMI+

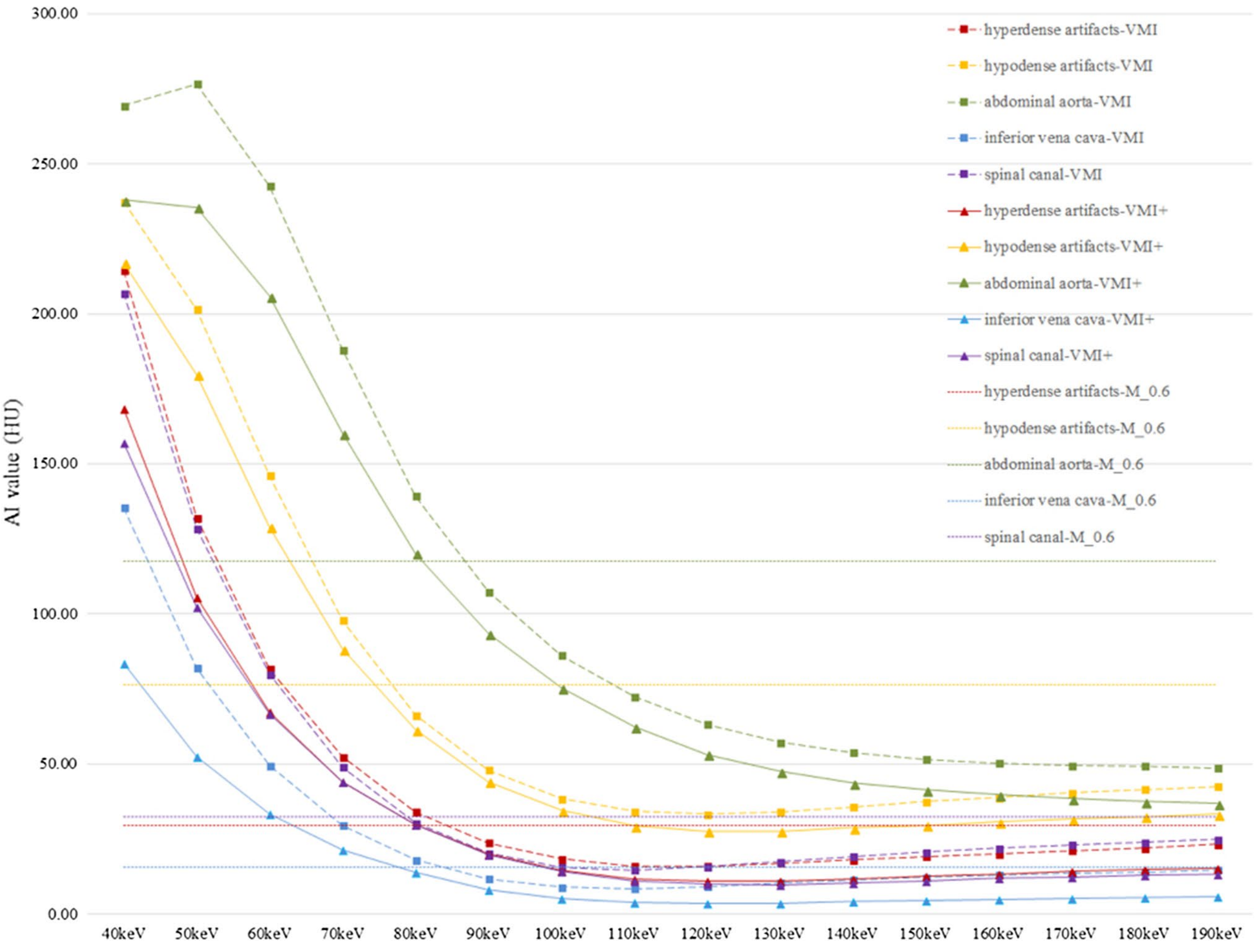

Fig. 2 The variation trends of AI values at all of the energy levels for five ROIs. The curves for VMI and VMI+ in the hyperdense artefacts, hypodense artefacts, spinal canal and IVC show sharp decline before the 120 keV or 130 keV, and slowly rise after then. But the continuous decrease trend is performed on the curve for VMI and VMI+ in the AA. No matter where ROIs were drawn and what energy levels were selected, the calculated AI values in the VMI+ series were always lower than the VMI

algorithms at all energy levels compared to traditional VMI and standard M_0.6 reconstructions. The AI values were the lowest at 120 keV VMI+ in the hyperdense artefacts without significant differences compared to 130 keV VMI+; at 130 keV VMI+ in the hypodense artefacts, the spinal canal (where no significant difference was found compared to 120 keV VMI+), and the IVC; and at 190 keV VMI+ in the AA. The values were significantly lower compared to the M_0.6 and all the VMI series, with the exception of the hypodense artefacts. Furthermore, the highest subjective image quality was obtained at 130 keV in the metal–bone interface, the surrounding soft tissue, the IVC, and the AA, and at 120 keV VMI+ in the spinal canal. Excluding the AA, these scores were higher than the M_0.6 series and all the VMI series. These results indicate that metal artefacts can be suppressed efficiently at high-keV VMI+ , and the VMI+ reconstructions should be chosen over the M_0.6 and traditional VMI algorithms for patients with lumbar internal fixation who have undergone lumbar DECT scanning.

Previous studies confirmed that high-keV VMI reconstructions can effectively reduce beam-hardening artefacts and enhance the contrast between adjacent structures, because of images produced by projection-space data and generated at a range of photon energy levels [2, 27]. Different energy levels were recommended to improve image quality and diagnosis value, such as 105 keV for implants placed in the trunk of the body and the extremities; 130 keV for internal, external, and total metal orthopaedic implants; and 120 keV and even a range from 110 keV to 140 keV or from 123 keV to 141 keV for pedicle screws. Compared to standard linearly blended algorithms, VMI reconstructions were able to produce more images in a given time and obtain better objective and subjective evaluations of

Table 3 Results of qualitative image analysis

Image series	Metal–bone interface	Surrounding soft tissue	Spinal canal	AA	IVC
M_0.6	2.30 (1–3) [0.890]	2.67 (2–4) [0.766]	2.27 (1–4) [0.909]	2.58 (1–4) [0.826]	2.81 (1–4) [0.843]
VMI 40	1.03 (1–2) [0.740]	1.03 (1–2) [0.597]	1.04 (1–2) [0.663]	1.03 (1–2) [0.596]	1.05 (1–2) [0.650]
VMI+ 40	1.04 (1–2) [0.663]	1.27 (1–2) [0.604]	1.28 (1–3) [0.847]	1.20 (1–3) [0.671]	1.60 (1–3) [0.838]
VMI 50	1.05 (1–2) [0.853]	1.04 (1–2) [0.654]	1.07 (1–2) [0.701]	1.05 (1–2) [0.422]	1.13 (1–3) [0.639]
VMI+ 50	1.09 (1–2) [0.705]	1.83 (1–3) [0.578]	1.59 (1–3) [0.898]	1.37 (1–3) [0.834]	2.04 (1–4) [0.889]
VMI 60	1.14 (1–2) [0.817]	1.78 (1–3) [0.566]	1.34 (1–3) [0.770]	1.28 (1–2) [0.667]	1.65 (1–3) [0.814]
VMI+ 60	1.73 (1–2) [0.572]	2.16 (1–3) [0.580]	2.15 (1–4) [0.882]	1.73 (1–3) [0.789]	2.60 (1–4) [0.885]
VMI 70	1.16 (1–2) [0.842]	2.13 (1–4) [0.626]	1.76 (1–3) [0.879]	1.73 (1–3) [0.616]	2.21 (1–4) [0.738]
VMI+ 70	2.13 (1–3) [0.654]	2.53 (2–4) [0.675]	2.83 (2–4) [0.854]	2.03 (1–4) [0.857]	3.02 (1–4) [0.894]
VMI 80	2.02 (1–3) [0.653]	2.58 (2–4) [0.648]	2.40 (1–4) [0.874]	2.16 (1–4) [0.718]	2.73 (2–4) [0.856]
VMI+ 80	2.62 (2–4) [0.694]	2.86 (2–4) [0.718]	3.26 (2–4) [0.805]	2.44 (1–4) [0.836]	3.34 (2–5) [0.887]
VMI 90	2.59 (1–4) [0.809]	3.04 (2–4) [0.825]	3.06 (2–4) [0.830]	2.62 (2–4) [0.803]	3.17 (2–5) [0.826]
VMI+ 90	3.05 (2–4) [0.553]	3.20 (2–4) [0.517]	3.71 (3–5) [0.779]	2.81 (2–4) [0.758]	3.59 (2–5) [0.871]
VMI 100	3.08 (2–4) [0.833]	3.37 (3–4) [0.571]	3.82 (3–5) [0.668]	3.02 (2–4) [0.794]	3.62 (2–5) [0.856]
VMI+ 100	3.08 (3–5) [0.675]	3.53 (3–4) [0.551]	4.16 (3–5) [0.512]	3.24 (2–4) [0.757]	3.88 (2–5) [0.869]
VMI 110	3.69 (3–5) [0.796]	3.82 (3–5) [0.529]	4.29 (3–5) [0.813]	3.34 (2–5) [0.788]	3.98 (2–5) [0.789]
VMI+ 110	3.62 (3–5) [0.736]	3.83 (3–5) [0.719]	4.52 (4–5) [0.536]	3.52 (2–5) [0.815]	4.09 (2–5) [0.778]
VMI 120	4.09 (3–5) [0.668]	4.23 (3–5) [0.760]	4.73 (4–5) [0.651]	3.64 (2–5) [0.885]	4.18 (2–5) [0.891]
VMI+ 120	4.34 (3–5) [0.823]	4.25 (3–5) [0.754]	**4.87** (4–5) [0.639]	3.79 (2–5) [0.879]	4.35 (2–5) [0.863]
VMI 130	4.25 (3–5) [0.722]	4.31 (3–5) [0.710]	4.43 (4–5) [0.721]	3.79 (2–5) [0.869]	4.27 (2–5) [0.749]
VMI+ 130	**4.60** (4–5) [0.704]	**4.45** (3–5) [0.608]	4.50 (4–5) [0.619]	**4.03** (2–5) [0.864]	**4.50** (3–5) [0.762]
VMI 140	4.04 (3–5) [0.535]	4.05 (3–5) [0.651]	4.02 (3–5) [0.666]	3.84 (2–5) [0.771]	4.12 (2–5) [0.698]
VMI+ 140	4.23 (4–5) [0.583]	4.23 (3–5) [0.700]	4.07 (3–5) [0.536]	4.02 (2–5) [0.758]	4.22 (3–5) [0.649]
VMI 150	3.81 (3–5) [0.654]	3.92 (3–5) [0.570]	3.86 (3–5) [0.541]	3.79 (2–5) [0.705]	4.00 (2–5) [0.647]
VMI+ 150	4.05 (3–5) [0.600]	4.03 (3–5) [0.569]	3.94 (3–5) [0.685]	3.98 (2–5) [0.700]	4.06 (2–5) [0.713]
VMI 160	3.64 (3–5) [0.577]	3.69 (3–4) [0.530]	3.60 (3–4) [0.680]	3.79 (2–5) [0.697]	3.90 (2–5) [0.728]
VMI+ 160	3.93 (3–5) [0.747]	3.88 (3–5) [0.656]	3.79 (3–4) [0.846]	3.91 (2–5) [0.782]	3.93 (2–5) [0.666]
VMI 170	3.31 (3–4) [0.567]	3.39 (3–4) [0.654]	3.34 (3–4) [0.642]	3.61 (1–5) [0.747]	3.70 (2–5) [0.459]
VMI+ 170	3.73 (3–5) [0.616]	3.58 (3–4) [0.617]	3.56 (3–4) [0.803]	3.85 (1–5) [0.694]	3.87 (2–5) [0.783]
VMI 180	3.08 (3–4) [0.726]	3.15 (2–4) [0.518]	3.07 (2–4) [0.740]	3.43 (1–5) [0.697]	3.35 (2–4) [0.595]
VMI+ 180	3.46 (3–4) [0.776]	3.25 (2–4) [0.547]	3.28 (2–4) [0.857]	3.74 (1–5) [0.523]	3.76 (2–5) [0.674]
VMI 190	3.05 (2–4) [0.810]	2.97 (2–4) [0.608]	3.00 (2–4) [0.537]	3.30 (1–5) [0.681]	3.24 (2–4) [0.725]
VMI+ 190	3.38 (3–4) [0.873]	3.11 (2–4) [0.577]	3.11 (2–4) [0.662]	3.61 (1–5) [0.548]	3.60 (2–5) [0.767]

Data are recorded as mean with range of rating scores in parenthesis and ICC value in square brackets in all of the image series to perform subjective image quality of the five objects

Highest rating scores are in bold for each dataset

metal artefacts reduction at high-keV [2, 3, 13–15, 17]. In addition, one of studies evaluated the artefacts reduction by using the VMI reconstructions for the individual structures around metal implants of posterior spinal fusion. The corresponding energy level for the optimal image quality of each structure was recommended, such as 200 keV for the implant inheriting bone and the spinal canal, 160 keV for the muscle, and 180 keV for the aorta. However, these energy levels are generally higher than the energy levels in the VMI+ that we recommended. The differences may be related to the characteristics of the VMI+ at a relatively lower energy level, combining the advantages of the VMI reconstructions including low noise at optimal energy levels and high contrast at low energy levels [17]. Furthermore, the VMI technique combined with metal artefact reduction software (MARS) as another reconstruction technique to diminish metal artefacts has been introduced [8, 12]. A prior study reported that DECT with MARS decreased metallic artefacts and enhanced the sharpness of dental prostheses and nearby regions [12]. However, this reconstruction technique can distort the pedicle screw [15]. Breaking and loosening of metal implants can be challenging. It was also reported that the competence of MARS in reducing metal artefacts depended on an implant's shape, size, and composition. It was more

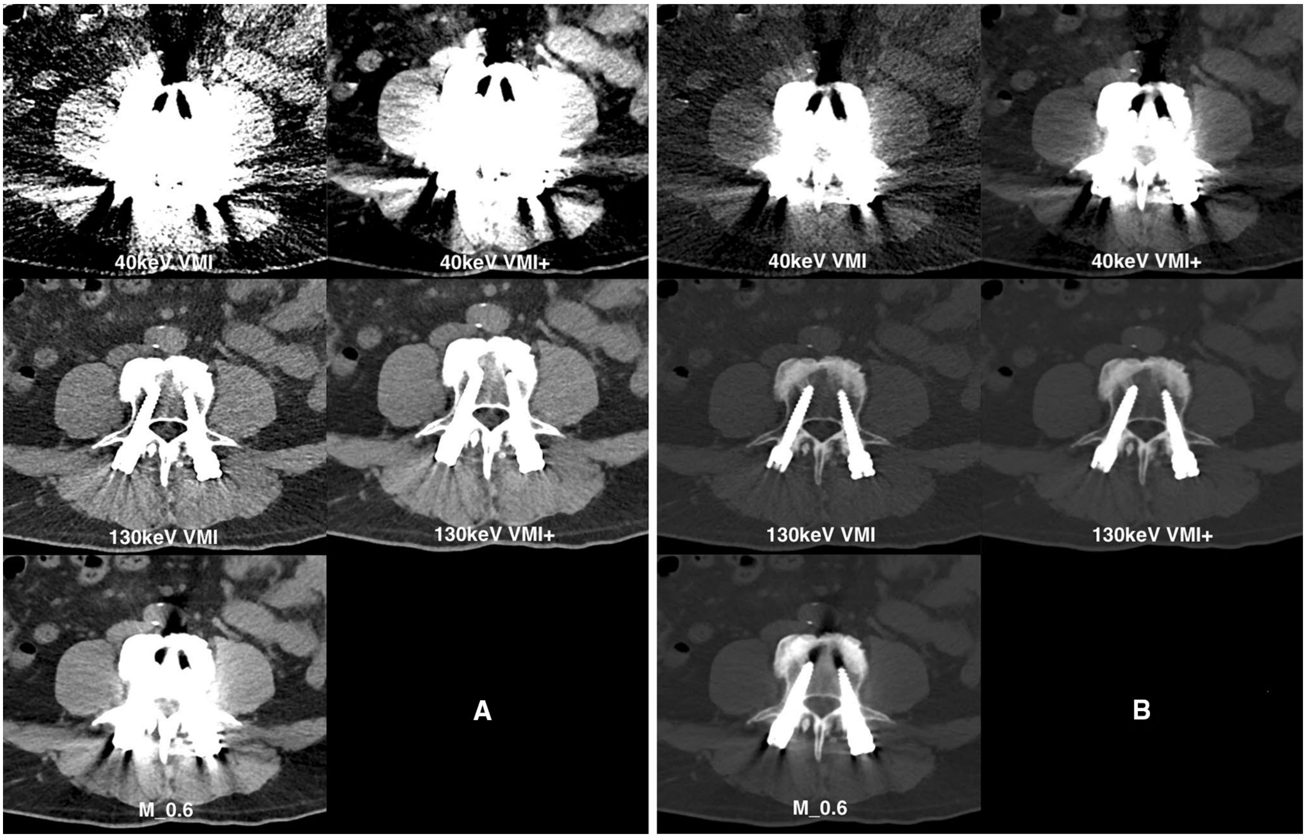

Fig. 3 Images of a patient at the M_0.6, 40 keV and 130 keV VMI as well as VMI+ . Images obtained in a 59-year-old male patient with lumbar metal internal fixation. Axial images were reconstructed with soft tissue window (**a**) and bone window (**b**) in the 40 keV VMI, 40 keV VMI+, 130 keV VMI, 130 keV VMI+, and M_0.6. The obvious decrease in artefacts is seen on the 130 keV VMI+ images in direct comparison with the M_0.6 and the low-keV VMI or VMI+ images. And the best images quality was obtained in the 130 keV VMI+

effective than titanium for the replacement of major joints and dense metal [2, 28, 29].

Noise-optimised VMI+ reconstruction was performed using the frequency split and recombination technique, which combines the advantages of high contrast at low keV and minimum image noise at optimal keV [30]. Studies have reported that tumour and vessels image quality was superior at low energy levels [18–25]. The current study aimed to close the research gap for VMI+ reconstructions on metal artefact reduction, evaluate the effects at energy levels from 40 keV to 190 keV, and recommend the optimal energy levels according to different ROIs. Similar to prior image post-processing techniques, metal artefacts did not completely disappear but were continuously reduced, and this was more apparent at high-keV energy levels. However, the AI values were significantly lower and the subjective image quality assessments were superior at both optimal energy levels compared to the M_0.6 images and all the VMI algorithms in most of the ROIs. Only in the hypodense artefacts, there was no significant difference in the AI values between 130 keV VMI+ and 120 keV VMI, and a subjective evaluation of the AA disturbed mainly by hypodense streaks showed no significant differences between 190 keV VMI+ and 190 keV VMI. Therefore, we posit that the effect of VMI+ reconstructions in minimising beam-hardening artefacts is superior at reducing artefacts from photon starvation, similar to VMI. In contrast to the current research, the 40 keV VMI+ reconstruction was recommended to optimise the image quality of DE-CTA of the aorta and abdominal vessels in initial studies [18, 21, 23], but these vessels contained iodinated contrast media unobstructed by metal artefacts. Combined with the results of the present study, it was deduced that high-keV (≥ 130 keV) VMI+ reconstructions can reduce more metal artefacts and provide better image quality for AA without contrast media compared to low-keV VMI+ reconstructions. The VMI+ energy level for optimal image quality of AA disturbed by metal artefacts with or without contrast media should be assessed in the future studies.

This study has some limitations. First, a relatively small number of patients with lumbar metal internal fixation were obtained over the course of 10 months. Second, this study did not discriminate according to different metal components, despite the fact that most of the implants were titanium alloy. Varying shapes and compositions of each type of titanium alloy may result in different effects in reducing metal artefacts via post-processing techniques. Finally, this report focused only on lumbar internal instrumentation and did not assess other metal fixtures at different body parts. Further research is therefore necessary.

In summary, this study confirmed that the VMI+ technique decreases metal artefacts of lumbar internal fixation and improves image quality. To observe the metal–bone interface, surrounding soft tissues, and IVC after lumbar internal fixation surgery, the 130 keV VMI+ should be reconstructed. If a spinal canal disease is suspected, 120 keV VMI+ reconstruction should be applied to optimise the image quality and improve the diagnostic performance. Although the high-keV (≥ 130 keV) VMI+ reconstruction for AA imaging with metal artefacts was previously mentioned, further research on AA disease covered by lumbar fixation artefacts is warranted.

Acknowledgements This study was supported by the National Key Research and Development Program of China (Grant No. 2016YFA0203700), Shanghai Rising-Star Program (Grant No. 16QA1400900), Grant from the Shanghai Municipal Commission of Health and Family Planning (Grant No. 2017BR003).

Compliance with ethical standards

Conflict of interest The authors declare that they have no conflict of interest.

References

1. Douglas-Akinwande AC, Buckwalter KA, Rydberg J, Rankin JL, Choplin RH (2006) Multichannel CT: evaluating the spine in postoperative patients with orthopedic hardware. Radiographics 26(Suppl 1):S97–S110. https://doi.org/10.1148/rg.26si065512
2. Pessis E, Campagna R, Sverzut JM, Bach F, Rodallec M, Guerini H, Feydy A, Drape JL (2013) Virtual monochromatic spectral imaging with fast kilovoltage switching: reduction of metal artifacts at CT. Radiographics 33:573–583. https://doi.org/10.1148/rg.332125124
3. Bamberg F, Dierks A, Nikolaou K, Reiser MF, Becker CR, Johnson TR (2011) Metal artifact reduction by dual energy computed tomography using monoenergetic extrapolation. Eur Radiol 21:1424–1429. https://doi.org/10.1007/s00330-011-2062-1
4. Amato V, Giannachi L, Irace C, Corona C (2010) Accuracy of pedicle screw placement in the lumbosacral spine using conventional technique: computed tomography postoperative assessment in 102 consecutive patients. J Neurosurg Spine 12:306–313. https://doi.org/10.3171/2009.9.spine09261
5. Okuda S, Miyauchi A, Oda T, Haku T, Yamamoto T, Iwasaki M (2006) Surgical complications of posterior lumbar interbody fusion with total facetectomy in 251 patients. J Neurosurg Spine 4:304–309. https://doi.org/10.3171/spi.2006.4.4.304
6. Rosenberg WS, Mummaneni PV (2001) Transforaminal lumbar interbody fusion: technique, complications, and early results. Neurosurgery 48:569–574; discussion 574–565
7. Rajaraman V, Vingan R, Roth P, Heary RF, Conklin L, Jacobs GB (1999) Visceral and vascular complications resulting from anterior lumbar interbody fusion. J Neurosurg 91:60–64
8. Lambert JW, Edic PM, FitzGerald PF, Torres AS, Yeh BM (2015) Complementary contrast media for metal artifact reduction in dual-energy computed tomography. J Med Imaging (Bellingham) 2:033503. https://doi.org/10.1117/1.jmi.2.3.033503
9. Grosse Hokamp N, Neuhaus V, Abdullayev N, Laukamp K, Lennartz S, Mpotsaris A, Borggrefe J (2018) Reduction of artifacts caused by orthopedic hardware in the spine in spectral detector CT examinations using virtual monoenergetic image reconstructions and metal-artifact-reduction algorithms. Skeletal Radiol 47:195–201. https://doi.org/10.1007/s00256-017-2776-5
10. Barrett JF, Keat N (2004) Artifacts in CT: recognition and avoidance. Radiographics 24:1679–1691. https://doi.org/10.1148/rg.246045065
11. Lee MJ, Kim S, Lee SA, Song HT, Huh YM, Kim DH, Han SH, Suh JS (2007) Overcoming artifacts from metallic orthopedic implants at high-field-strength MR imaging and multi-detector CT. Radiographics 27:791–803. https://doi.org/10.1148/rg.273065087
12. Cha J, Kim HJ, Kim ST, Kim YK, Kim HY, Park GM (2017) Dual-energy CT with virtual monochromatic images and metal artifact reduction software for reducing metallic dental artifacts. Acta Radiol 58:1312–1319. https://doi.org/10.1177/0284185117692174
13. Dong Y, Shi AJ, Wu JL, Wang RX, Sun LF, Liu AL, Liu YJ (2016) Metal artifact reduction using virtual monochromatic images for patients with pedicle screws implants on CT. Eur Spine J 25:1754–1763. https://doi.org/10.1007/s00586-015-4053-4
14. Zhou C, Zhao YE, Luo S, Shi H, Li L, Zheng L, Zhang LJ, Lu G (2011) Monoenergetic imaging of dual-energy CT reduces artifacts from implanted metal orthopedic devices in patients with factures. Acad Radiol 18:1252–1257. https://doi.org/10.1016/j.acra.2011.05.009
15. Wang Y, Qian B, Li B, Qin G, Zhou Z, Qiu Y, Sun X, Zhu B (2013) Metal artifacts reduction using monochromatic images from spectral CT: evaluation of pedicle screws in patients with scoliosis. Eur J Radiol 82:e360–e366. https://doi.org/10.1016/j.ejrad.2013.02.024
16. Kuchenbecker S, Faby S, Sawall S, Lell M, Kachelriess M (2015) Dual energy CT: how well can pseudo-monochromatic imaging reduce metal artifacts? Med Phys 42:1023–1036. https://doi.org/10.1118/1.4905106
17. Dangelmaier J, Schwaiger BJ, Gersing AS, Kopp FF, Sauter A, Renz M, Riederer I, Braren R, Pfeiffer D, Fingerle A, Rummeny EJ, Noel PB (2018) Dual layer computed tomography: reduction of metal artefacts from posterior spinal fusion using virtual monoenergetic imaging. Eur J Radiol 105:195–203. https://doi.org/10.1016/j.ejrad.2018.05.034
18. Frellesen C, Kaup M, Wichmann JL, Husers K, Scholtz JE, Albrecht MH, Metzger SC, Bauer RW, Kerl JM, Lehnert T, Vogl TJ, Bodelle B (2016) Noise-optimized advanced image-based virtual monoenergetic imaging for improved visualization of lung cancer: comparison with traditional virtual monoenergetic imaging. Eur J Radiol 85:665–672. https://doi.org/10.1016/j.ejrad.2015.12.022
19. Wichmann JL, Gillott MR, De Cecco CN, Mangold S, Varga-Szemes A, Yamada R, Otani K, Canstein C, Fuller SR, Vogl TJ, Todoran TM, Schoepf UJ (2016) Dual-energy computed tomography angiography of the lower extremity runoff: impact of noise-optimized virtual monochromatic imaging on image quality and diagnostic accuracy. Invest Radiol 51:139–146. https://doi.org/10.1097/rli.0000000000000216

20. Martin SS, Pfeifer S, Wichmann JL, Albrecht MH, Leithner D, Lenga L, Scholtz JE, Vogl TJ, Bodelle B (2017) Noise-optimized virtual monoenergetic dual-energy computed tomography: optimization of kiloelectron volt settings in patients with gastrointestinal stromal tumors. Abdom Radiol (NY) 42:718–726. https://doi.org/10.1007/s00261-016-1011-5
21. Martin SS, Albrecht MH, Wichmann JL, Husers K, Scholtz JE, Booz C, Bodelle B, Bauer RW, Metzger SC, Vogl TJ, Lehnert T (2017) Value of a noise-optimized virtual monoenergetic reconstruction technique in dual-energy CT for planning of transcatheter aortic valve replacement. Eur Radiol 27:705–714. https://doi.org/10.1007/s00330-016-4422-3
22. Martin SS, Wichmann JL, Weyer H, Scholtz JE, Leithner D, Spandorfer A, Bodelle B, Jacobi V, Vogl TJ, Albrecht MH (2017) Endoleaks after endovascular aortic aneurysm repair: improved detection with noise-optimized virtual monoenergetic dual-energy CT. Eur J Radiol 94:125–132. https://doi.org/10.1016/j.ejrad.2017.06.017
23. Martin SS, Wichmann JL, Pfeifer S, Leithner D, Lenga L, Reynolds MA, D'Angelo T, Hammerstingl R, Gruber-Rouh T, Vogl TJ, Albrecht MH (2017) Impact of noise-optimized virtual monoenergetic dual-energy computed tomography on image quality in patients with renal cell carcinoma. Eur J Radiol 97:1–7. https://doi.org/10.1016/j.ejrad.2017.10.008
24. Leithner D, Mahmoudi S, Wichmann JL, Martin SS, Lenga L, Albrecht MH, Booz C, Arendt CT, Beeres M, D'Angelo T, Bodelle B, Vogl TJ, Scholtz JE (2018) Evaluation of virtual monoenergetic imaging algorithms for dual-energy carotid and intracerebral CT angiography: effects on image quality, artefacts and diagnostic performance for the detection of stenosis. Eur J Radiol 99:111–117. https://doi.org/10.1016/j.ejrad.2017.12.024
25. De Cecco CN, Caruso D, Schoepf UJ, De Santis D, Muscogiuri G, Albrecht MH, Meinel FG, Wichmann JL, Burchett PF, Varga-Szemes A, Sheafor DH, Hardie AD (2018) A noise-optimized virtual monoenergetic reconstruction algorithm improves the diagnostic accuracy of late hepatic arterial phase dual-energy CT for the detection of hypervascular liver lesions. Eur Radiol 28:3393–3404. https://doi.org/10.1007/s00330-018-5313-6
26. Albrecht MH, Trommer J, Wichmann JL, Scholtz JE, Martin SS, Lehnert T, Vogl TJ, Bodelle B (2016) Comprehensive comparison of virtual monoenergetic and linearly blended reconstruction techniques in third-generation dual-source dual-energy computed tomography angiography of the thorax and abdomen. Invest Radiol 51:582–590. https://doi.org/10.1097/rli.0000000000000272
27. Kaza RK, Platt JF, Cohan RH, Caoili EM, Al-Hawary MM, Wasnik A (2012) Dual-energy CT with single- and dual-source scanners: current applications in evaluating the genitourinary tract. Radiographics 32:353–369. https://doi.org/10.1148/rg.322115065
28. Lee YH, Park KK, Song HT, Kim S, Suh JS (2012) Metal artefact reduction in gemstone spectral imaging dual-energy CT with and without metal artefact reduction software. Eur Radiol 22:1331–1340. https://doi.org/10.1007/s00330-011-2370-5
29. Brook OR, Gourtsoyianni S, Brook A, Mahadevan A, Wilcox C, Raptopoulos V (2012) Spectral CT with metal artifacts reduction software for improvement of tumor visibility in the vicinity of gold fiducial markers. Radiology 263:696–705. https://doi.org/10.1148/radiol.12111170
30. Grant KL, Flohr TG, Krauss B, Sedlmair M, Thomas C, Schmidt B (2014) Assessment of an advanced image-based technique to calculate virtual monoenergetic computed tomographic images from a dual-energy examination to improve contrast-to-noise ratio in examinations using iodinated contrast media. Invest Radiol 49:586–592. https://doi.org/10.1097/rli.0000000000000060

Affiliations

Yanwei Zeng[1,2] · Kai Deng[3] · Haitao Yang[3] · Yi Tan[3] · Jun Liu[3] · Daoying Geng[1,2] · Jun Zhang[1,2]

✉ Jun Liu
junliu123@csu.edu.cn

✉ Jun Zhang
zhj81828@163.com

Yanwei Zeng
18211220088@fudan.edu.cn

Kai Deng
523256501@qq.com

Haitao Yang
Shepherdyht@csu.edu.cn

Yi Tan
252565944@qq.com

Daoying Geng
GengdaoyingGDY@163.com

[1] Department of Radiology, Huashan Hospital,
Fudan University, No.12 Wulumuqi Road (Middle),
Shanghai 200040, China

[2] Institute of Functional and Molecular Medical Imaging,
Fudan University, No.12 Wulumuqi Road (Middle),
Shanghai 200040, China

[3] Department of Radiology, Second Xiangya Hospital, Central
South University, Changsha 410011, China